



Pyroxene microstructure in the Northwest Africa 856 martian meteorite

Hugues LEROUX,^{1*} Bertrand DEVOUARD,² Patrick CORDIER,¹ and François GUYOT³

¹Laboratoire de Structure et Propriétés de l'Etat Solide - UMR 8008, Université des Sciences et Technologies de Lille, F-59655 Villeneuve d'Ascq-Cedex France

²Laboratoire Magmas et Volcans - UMR 6524, Université Blaise Pascal - CNRS - OPGC, 5, rue Kessler, F-63038 Clermont-Ferrand, France

³Laboratoire de Minéralogie-Cristallographie and Institut de Physique du Globe de Paris - UMR 7590, Tour 16, Case 115, 4 place Jussieu, F-75252 Paris 05, France

*Corresponding author. E-mail: Hugues.Leroux@univ-lille1.fr

(Received 18 February 2004; revision accepted 23 March 2004)

Abstract—Transmission electron microscopy was used to examine pyroxene microstructure in the Northwest Africa (NWA) 856 martian meteorite to construct its cooling and shock histories. All pyroxenes contain strained coherent pigeonite/augite exsolution lamellae on (001). The average width and periodicity of lamellae are 80 and 400 nm, respectively, indicating a cooling rate below 0.1 °C/hr for the parent rock. Pigeonite and augite are topotactic, with strained coherent interfaces parallel to (001). The closure temperature for Ca-Fe, Mg interdiffusion, estimated from the composition at the augite pigeonite interface, is about 700 °C. Tweed texture in augite reveals that a spinodal decomposition occurred. Locally, tweed evolved toward secondary pigeonite exsolution lamellae on (001). Due to the decreasing diffusion rate with decreasing temperature, “M-shaped” concentration profiles developed in augite lamellae. Pigeonite contains antiphase boundaries resulting from the C2/c to P2₁/c space group transition that occurred during cooling. The reconstructive phase transition from P2₁/c clinopyroxene to orthopyroxene did not occur. The deformation (shock) history of the meteorites is revealed by the presence of dislocations and mechanical twins. Dislocations are found in glide configuration, with the [001](100) glide system preferentially activated. They exhibit strong interaction with the strained augite/pigeonite interfaces and did not propagate over large distances. Twins are found to be almost all parallel to (100) and show moderate interaction with the augite/pigeonite interfaces. These twins are responsible for the plastic deformation of the pyroxene grains. Comparison with microstructure of shocked clinopyroxene (experimentally or naturally shocked) suggests that NWA 856 pyroxenes are not strongly shocked.

INTRODUCTION

The basaltic shergottites are igneous rocks crystallized from lava. These rocks are predominantly composed of pyroxenes (augite and pigeonite) and plagioclase (converted into maskelynite by shock). Crystal shape and size, phase composition, and chemical zoning of the minerals are the results of one or several magmatic events. Minerals in martian meteorites are also found to be severely shocked due to their ejection from the planet's surface by large-scale impacts. Thermal and shock histories are, thus, superimposed in martian minerals.

Pyroxene composition and microstructure are useful indicators of thermal and deformation history in meteorites.

Thermal history can be deciphered from chemical zoning formed during crystallization of the parent magma (e.g., Miyamoto et al. 2001) and also by subsolidus phase transformations, for instance, the formation and coarsening of augite and pigeonite intergrowths (e.g., Grove 1982; Müller 1991; Weinbruch et al. 2001) or the degree of cation ordering (Zema et al. 1997). Pyroxenes are also good records of shock deformation, which induces such crystal defects as dislocations, planar features, and mechanical twins (e.g., Mori and Takeda 1983; Müller 1993; Leroux 2001).

This work uses a combination of transmission and analytical electron microscopy to study pyroxene microstructure in the NWA 856 martian meteorite to unravel the thermal and shock histories of its parent rock.

SAMPLE AND EXPERIMENTAL METHOD

The martian meteorite NWA 856 is a basaltic shergottite mainly composed of strongly zoned pyroxenes (augite and pigeonite) and plagioclase converted to maskelynite. Augite and pigeonite are present as separated grains. Extensive fractures, shock melt pockets, dense silica glass, and stishovite are also present (Jambon et al. 2002), indicating that the meteorite is strongly shocked. A detailed petrological and chemical study of the meteorite has been published by Jambon et al. (2002).

Pyroxene grains were selected based on optical examination of 30 μm -thick sections of the meteorite. Each sample was glued to a 3 mm-diameter copper aperture TEM grid and was ion-milled to electron transparency at 5 kV with an incident beam angle of 15° . The samples were coated with a thin carbon layer to promote conduction. Microstructure was investigated with a transmission electron microscope (TEM) Philips CM30, operating at 300 kV. Some complementary micrographs were obtained on a Jeol 2000FX TEM, operated at 200 kV. The defect structure was studied by conventional bright field and dark field modes, mainly using two beam diffraction conditions. Selected area electron diffraction (SAED) was used to investigate the crystallographic features of the microstructures. Quantitative chemical analyses were collected using an EDS (energy dispersive spectroscopy) attachment in the STEM mode (scanning transmission electron microscopy). X-rays were detected using a Noran Si detector with an ultrathin window. Concentrations were obtained using the Vantage software (version 2.3.2). K-factors were experimentally determined by the parameterless method (Van Cappellen 1990) using silicate standards. Thickness determination for the absorption correction procedure was based on the principle of electroneutrality (Van Cappellen and Doukhan 1994). When recording the concentration profiles performed across augite/pigeonite boundaries, attempts were made to obtain compositions with minimum overlap effects by orienting the interfaces parallel to the electron beam.

RESULTS

Augite-Pigeonite Exsolutions

Pyroxenes in NWA 856 consist of augite, $\text{En}_{46-26}\text{Wo}_{34-29}\text{Fs}_{21-43}$, and pigeonite, $\text{En}_{61-16}\text{Wo}_{9-22}\text{Fs}_{26-68}$ (Jambon et al. 2002). They display zoning from Mg-rich cores toward Fe-rich rims. As expected for eucritic or martian meteorites, both types of pyroxene grains are, in fact, composed of a sub- μm -scaled assemblage of augite and pigeonite, which results from subsolidus exsolution. Thus, the term “augite,” when applied to macroscopic grains, must be understood as a matrix of augite containing pigeonite exsolutions. Symmetrically, “pigeonite” grains are low-Ca CPX pyroxenes containing

augite exsolutions. At the TEM scale, these two-phase assemblages are clearly seen (Fig. 1a). Spacing between exsolved lamellae (i.e., the periodicity of the intergrowth) is variable, ranging from 80 nm to 1 μm (average about 400 nm). The average width of the exsolved augite or pigeonite lamellae is about 80 nm. The width and spacing of lamellae are closely related: the spacing is narrower when the lamellae are thinner. Lamellae are sometimes discontinuous, but they also can be interconnected, and some of them terminate as needles.

Augite and pigeonite are easily distinguished in the TEM by their SAED patterns. Augite belongs to the $C2/c$ space group, implying that the $h + k$ odd reflections are absent on SAED patterns. On the contrary, $h + k$ odd reflections are observed for pigeonite, which has a primitive unit cell and belongs to the $P2_1/c$ space group (Fig. 1b). SAED patterns also confirm the crystallographic relationship between pigeonite and augite. Their composition plane interface is close to the (001) lattice plane of both phases. The b^* and c^* directions coincide. Small differences of lattice parameters are also detected; $a_{\text{pig}} < a_{\text{aug}}$ and $c_{\text{pig}} < c_{\text{aug}}$, but $b_{\text{pig}} = b_{\text{aug}}$. Splitting of $h00$ reflections occurs due to the different monoclinic angles β , with $\Delta\beta \approx 3^\circ$ (Fig. 1b). This crystallographic misorientation is also visible on the direct images owing to the deflection of the (100) twins across the augite/pigeonite interfaces (Fig. 1c). Misfit dislocations were not observed at lamellae boundaries, showing that augite and pigeonite have a high degree of crystallographic coherence. However, there are considerable elastic strains at the interfaces as illustrated by the Bragg contrast across augite/pigeonite interfaces (Fig. 1d). Strain is due to the elastic deformation necessary to match the lattices of the two phases, which continually diverge during cooling. Coherency strain is also seen in SAED patterns recorded over one or several lamellae: plane bending results in streaking of the $h00^*$ spots in the c^* direction (see insert in Fig. 1b).

Compositions of augite and pigeonite intergrowths have been measured by TEM-EDS in the STEM mode using beam diameters of ~ 5 nm. Bulk compositions are in agreement with the petrographic study of Jambon et al. (2002). Composition ranges of the analyzed augite and pigeonite lamellae are $\text{En}_{22-32}\text{Wo}_{40-45}\text{Fs}_{23-37}$ and $\text{En}_{30-42}\text{Wo}_{4-7}\text{Fs}_{51-67}$, respectively (see Table 1 for representative compositions). These compositions do not significantly differ whether they are in augite-rich or in pigeonite-rich coarse-grained pyroxenes, implying that their relative proportion chiefly accounts for the bulk compositions of the pyroxene grains. Augite-pigeonite composition pairs are shown in Fig. 2a in the pyroxene quadrilateral. Figure 2b represents a simplified pseudobinary phase diagram corresponding to a vertical section in the pyroxene quadrilateral of Fig. 2a. In pigeonite-rich pyroxene grains, no composition gradient was detected. In contrast, composition profiles recorded in augite-rich pyroxenes display composition gradients in augite lamellae, with the highest Ca content near the augite/pigeonite

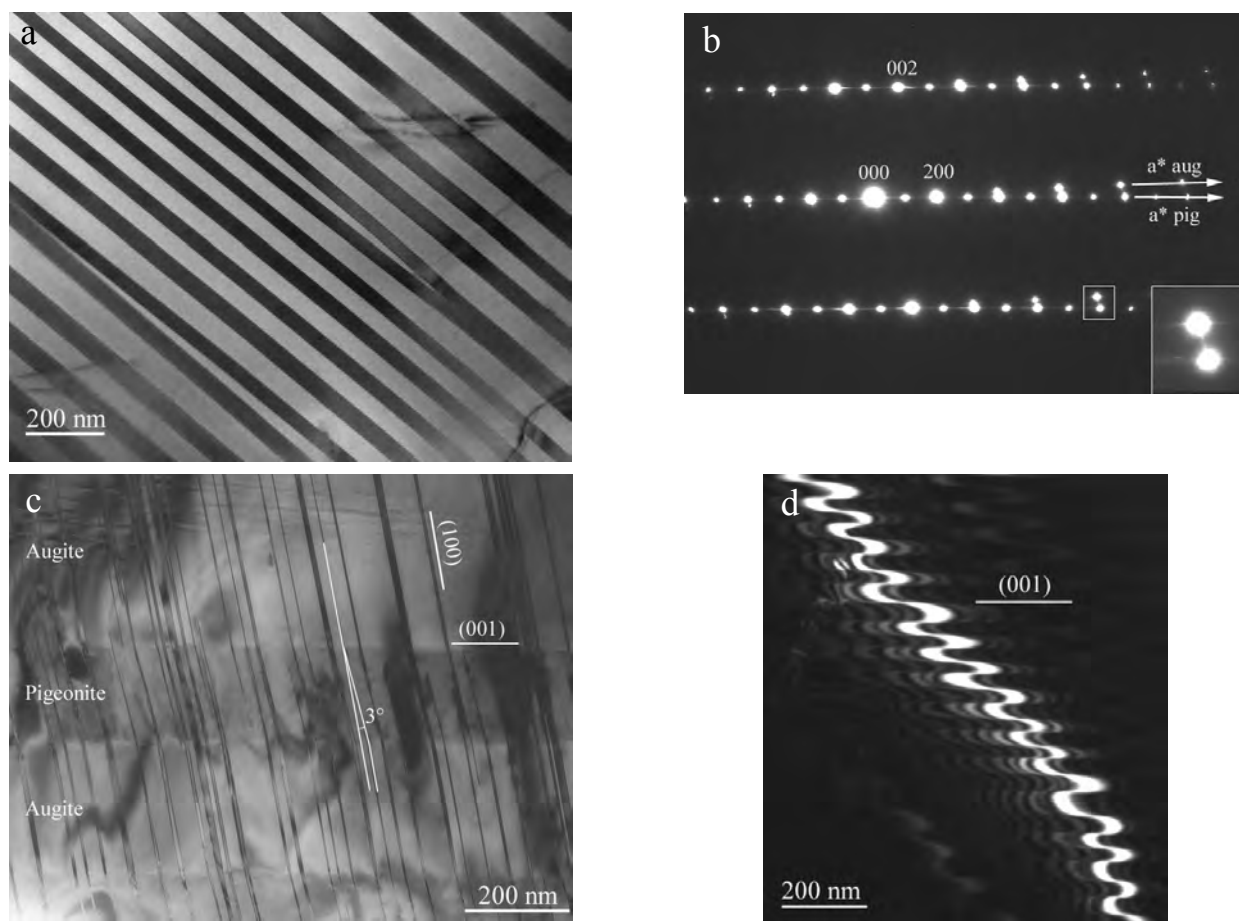


Fig. 1. a) TEM micrograph (bright field) of lamellar augite-pigeonite exsolutions on (001). Because of the Bragg condition used to make the image, augite appears in dark and pigeonite in bright. Note the interconnection of lamellae on the right side of the micrograph; b) selected area electron diffraction pattern of the above augite/pigeonite association, zone axis [010]. The two phases have a common c^* axis. The splitting of the spots on the $h0l$ rows (a^* direction) is due to the difference in the β angles of augite and pigeonite. Here, $\Delta\beta$ is about 3° . For augite, which belongs to the $C2/c$ space group, $h + k$ odd reflections are absent, while they are present for $P2_1/c$ pigeonite. Streaking parallel to a^* is due to the high density of narrow (100) twins present in the selected area. Evidence of lattice bending is also visible as streaks connecting the $h0l$ spots of pigeonite with those of augite (insert in the lower right corner); c) bright-field image taken with $g = 002$. The zone axis of the micrograph is close to [010]. (100) twins cross pigeonite lamellae in an augite matrix. Note the orientation change (of about 2°) of the twins inside the pigeonite lamellae; d) TEM dark field image taken with the 002 diffraction spot. Coherent interfaces between augite and pigeonite cause periodic strain and plane bending. It is illustrated here by a near sinusoidal Bragg line crossing the (001) pigeonite-augite alternation. The sinusoid wavelength corresponds to the augite-pigeonite periodicity in the Bragg line direction.

Table 1. Representative analyses of augite and pigeonite lamellae obtained by EDS (data in at%). Quantification includes the k-factors and the absorption corrections. Relative errors are about 2% for major elements (1σ).

	Pigeonite			Augite		
O	60.1	60.0	59.9	59.8	59.9	60.0
Si	20.0	19.8	19.7	19.5	19.8	19.9
Mg	8.0	5.8	7.6	4.4	6.0	6.1
Ca	1.15	1.16	1.21	8.3	8.6	8.4
Fe	10.1	12.6	10.9	7.4	4.5	4.7
Al	0.31	0.25	0.26	0.23	0.61	0.4
Cr	0.08	0.03	0.06	0.04	0.22	0.22
Ti	—	0.07	—	0.1	0.12	0.09
Mn	0.28	0.34	0.34	0.21	0.18	0.21
En %	42	30	39	22	31	32
Wo %	6	6	6	41	45	44
Fs %	52	64	55	37	23	24

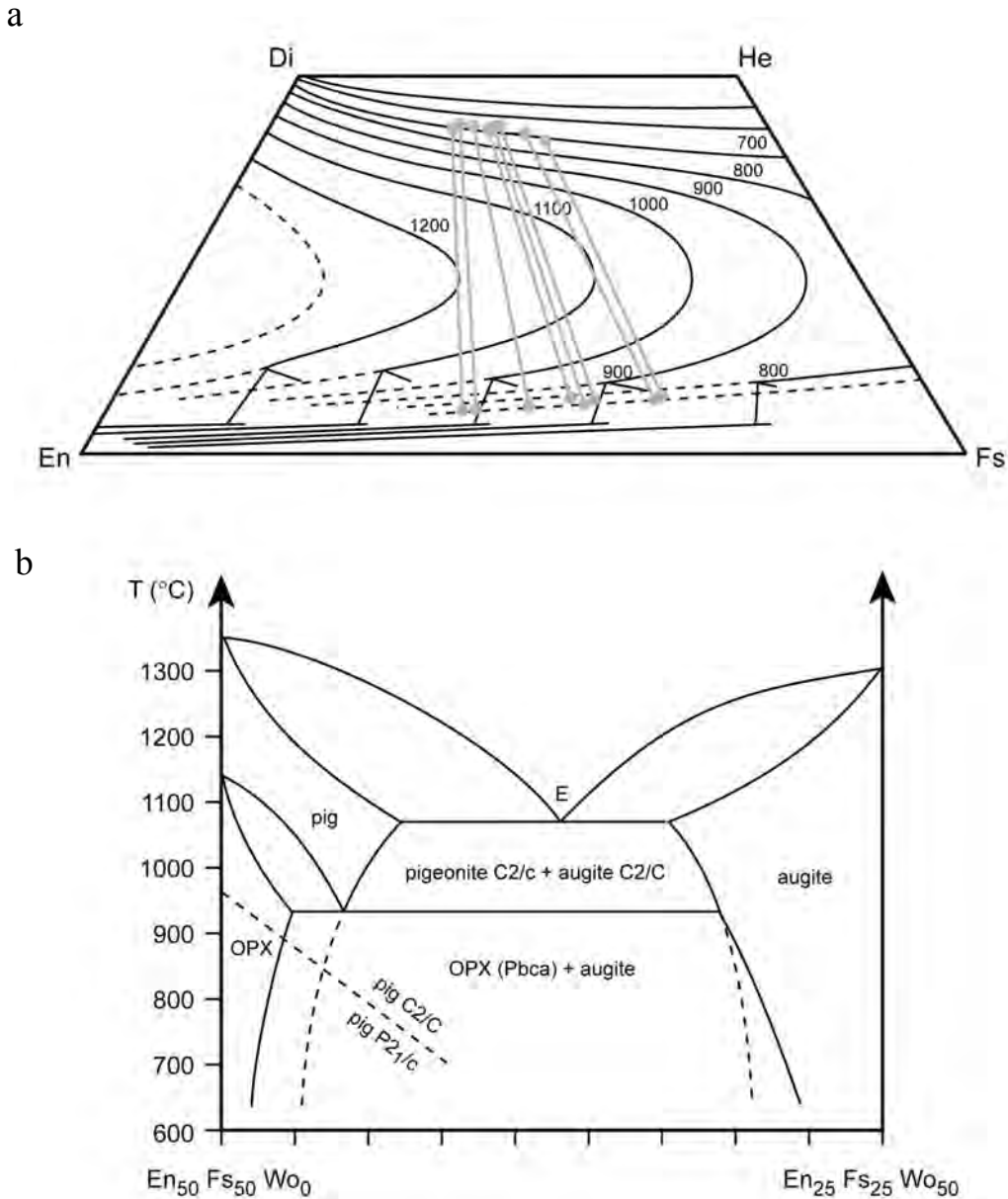


Fig. 2. a) Quadrilateral pyroxene composition diagram with solvus isotherms projected onto the quadrilateral at 800, 900, 1000, 1100, and 1200 °C (after Lindsley 1983). The gray lines represent tie-lines joining pairs of exsolved pigeonite and augite compositions, as determined by analytical TEM; b) simplified phase diagram corresponding to a vertical section at Fe/Mg = 1 in the pyroxene quadrilateral of (a) for low pressure conditions. The topology is in accordance with pseudobinary diagrams from Muir (1954), Yamakawa (1971), and Putnis (1992). The augite-pigeonite solvus position is after Lindsley (1983). The metastable solvus curve under about 950 °C is dashed. Temperatures of the C2/c to P2₁/c pigeonite phase transition were estimated from data in Prewitt et al. (1971). Solidus and liquidus temperatures, as well as the position of the eutectic (E) point, are indicative.

interfaces, and decrease from the rim to the middle of the augite domains (see Fig. 4b in the following section).

Tweed Texture and Secondary Pigeonite Exsolution in Augite

A fine and diffuse tweed texture was frequently observed in augite (Fig. 3a). The modulation appears as a fairly

periodic variation of contrast with diffuse boundaries. Its aspect strongly depends on diffraction conditions and small differences in sample orientation. Coarseness and sharpness also depend on the investigated area and may vary significantly over small distances. The contrast modulation is oriented close to (001) and (100). Modulated structure is generally more coarse within extended augite regions and absent near pigeonite exsolutions. The electron diffraction

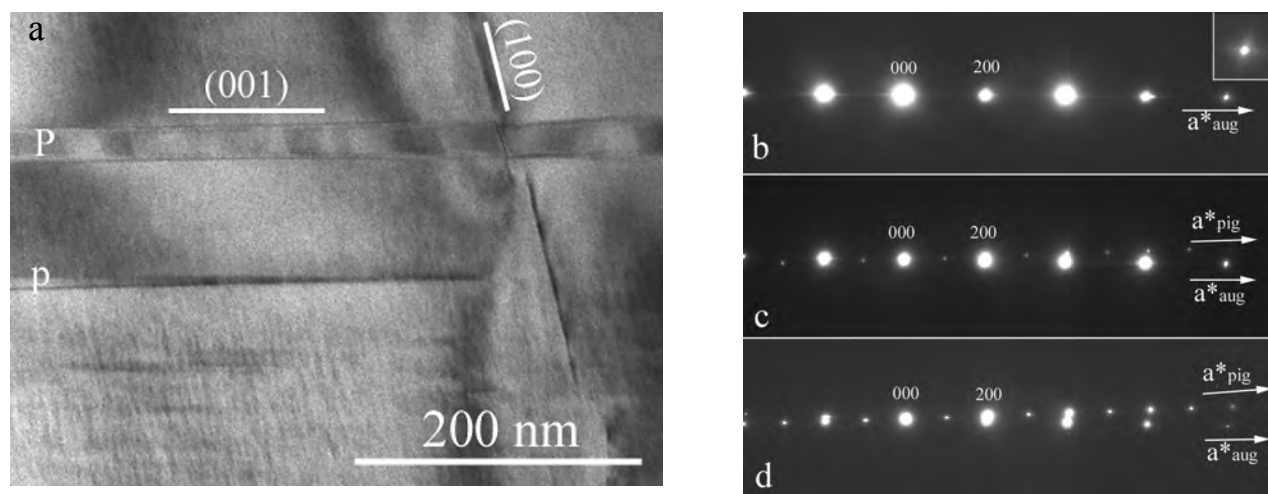


Fig. 3. a) Tweed texture in augite. The tweed contrast is parallel to (100) and (001). The variation of composition generates fluctuations of the local lattice spacing and orientation, visible here as periodic fluctuations of the diffraction contrast. Horizontal lamellae are pigeonite (P). One of the two is terminated as a needle. Bright field image, zone axis close to [010]; b) electron diffraction pattern from an area containing tweed structure, zone axis [010]. Only the $h00$ diffraction row is shown here. The absence of $h + k$ odd reflections indicates that the tweed structure contains only $C2/c$ space group pyroxene. Note the elongations along a^* and c^* (shown at high magnification in the insert), showing that the ($h00$) and the (001) lattice planes are elastically deformed; c) electron diffraction pattern along a^* from an area containing secondary pigeonite exsolution, such as shown in Fig. 4a. By comparison with (b), a set of $h + k$ odd reflections are now present, indicating $P2_1/c$ pigeonite in addition of $C2/c$ augite. The $\Delta\beta$ between the a^* directions of the two phases is about 2.5° . This relatively low $\Delta\beta$ angle probably indicates that the two phases are small and can accommodate reciprocally their lattices by elastic strain; d) for comparison with (b–c), the same diffraction pattern along a^* from an area containing primary augite/pigeonite intergrowth is given here. Note that the $\Delta\beta$ is higher (here 3.5°) than for secondary exsolutions. For this series (b–d) of diffraction patterns, streaking along (100) is due to the presence of (100) twins.

patterns reveal that tweed areas systematically retain the $C2/c$ structure, $h + k$ odd reflections being absent (Fig 3b). The absence of a two-phase microstructure is consistent with an unachieved spinodal decomposition mechanism, as previously interpreted (e.g., Buseck et al. 1980). Diffraction reflections also reveal spot elongations in directions close to a^* and c^* (see insert in Fig. 3b). This stretching of the diffraction spots is due to the elastic deformation between nano-scaled domains having different compositions (but the same structure), Ca-rich and Ca-poor domains having different cell parameters, and different monoclinic β angles.

In some areas, in particular where the augite lamellae are thick, the tweed microstructure appears to be continuous with secondary pigeonite exsolution lamellae. Spinodal decomposition, thus, is interpreted as being the formation mechanism for these second-stage lamellae. The secondary pigeonite exsolutions occur only in coarse augite lamellae and within the central area of these lamellae, while the regions near augite/pigeonite interfaces are free of them (Fig. 4a). On the diffraction patterns, splitting of the a^* direction (due to the difference of monoclinic angle β between augite and pigeonite) and the appearance of $h + k$ odd reflections indicate that the two distinct $C2/c$ and $P2_1/c$ phases are present (Fig. 3c). On Fig. 3d, a SAED pattern recorded on primary exsolutions is shown for comparison with Fig. 3c. They differ only by their intensities (related to phase proportions) and the difference between their monoclinic angles, $\Delta\beta$, which is smaller for the secondary pigeonite exsolutions.

Compositional profiles across primary and secondary pigeonite exsolutions have been recorded. They display a gradient in augite, the Ca content being higher near the primary augite/pigeonite interfaces and decreasing from the edges to the middle of the augite domains, where secondary pigeonite exsolution are present (Fig. 4b).

Antiphase Boundaries (APB) in Pigeonite

Pigeonite lamellae contain antiphase boundaries (APB) (Fig. 5a and 5b). An APB corresponds to an interface (planar defect) that separates two parts of a crystal by a mistake fault in the translational symmetry. In the case of pigeonite, the displacement vector across the APB is $1/2(a + b)$ (Morimoto and Tokonami 1969; Buseck et al. 1980). The antiphase domains (APD) can be easily imaged using dark field imaging with $h + k$ odd reflections. Antiphase domains have irregular morphologies, and their sizes strongly vary from place to place, from a few nm to 250 nm wide. In some areas, APBs appear to be preferentially oriented along (100), in particular, in pigeonite lamellae exsolved from primary augite (such a situation is visible in Fig. 7c). At the contact with augite lamellae, antiphase domains are found frequently more developed, suggesting that the augite/pigeonite interface is a nucleation site (Fig. 5c). These APDs are formed when pigeonite undergoes a displacive transformation with decreasing temperature from $C2/c$ to $P2_1/c$ structures (Morimoto and Tokonami 1969; Carpenter 1979; Buseck et

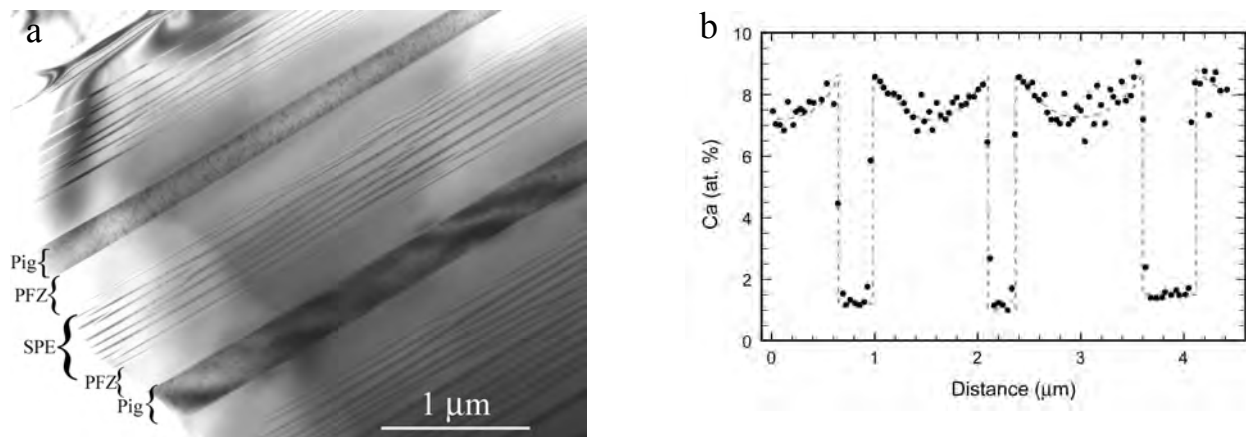


Fig. 4. a) Bright field image showing two generations of (001) pigeonite lamellae in augite. The secondary pigeonite exsolution lamellae correspond to the thin, irregular lamellae located in the middle of the augite band. Note the precipitate-free zone (PFZ) adjacent to the coarse pigeonite lamellae and the decreasing size of the secondary pigeonite exsolution (SPE) going toward these coarse pigeonite lamellae; b) composition profile perpendicular to (001) in an augite-rich grain containing primary and secondary pigeonite exsolution (similar to [a]). The profile tendency is underlined by a grey line. The central part of the “M-shaped” profile was supersaturated in Mg and Fe and a second generation of pigeonite exsolution occurred. On this figure, data are being scattered in the middle of augite lamellae because of the presence of these secondary pigeonite exsolution.

al. 1980; Tribaudino 2000). Unfortunately, antiphase domains are not reliable indicators of the cooling rate since their sizes and morphologies strongly depend on pyroxene composition (Carpenter 1979; Weinbruch et al. 2001).

Dislocations

Together with mechanical twins, dislocations are good indicators of shock deformation. Dislocations were not easy to image because of the presence of a tweed structure in augite, APBs in pigeonite, and strained pigeonite/augite interfaces. Their contrast was found to be reduced or superimposed on the thermal phase transformation microstructures. Dislocations were almost all found to have [001] Burgers vectors, suggesting that the glide system [001](100) was preferentially activated. Numerous dislocation sources are observed (Fig. 6a). The dislocations can originate from sources (e.g., Frank-Read) or from crack tips where the stress concentration is high. The dislocation density is not very high (average density 10^{13} to 10^{14} m⁻²). When dislocations cross augite/pigeonite interfaces, they strongly interact with them. Dislocation lines in augite are frequently found in contact and parallel to augite/pigeonite interfaces (Figs. 6b and 6c). Dislocations are pinned by the lamellae due to elastic interactions (Fig. 6d). Such configurations show that pigeonite lamellae are obstacles to dislocation propagation.

Twins

Pigeonite and augite grains display numerous (100) twins (Fig. 7a). These twins clearly shear (thus, postdate) the exsolution lamellae (Fig. 7) and are interpreted as mechanical

twins related to shock. Twin lamellae are evidenced by their orientation and by the additional reflections that appear on the diffraction patterns, according to the mirror twin law. Their density is highly heterogeneous within the examined grains. Some areas are free from twin lamellae, while in other areas, the density of twins is rather high (Fig. 7b), with average spacing between twin lamellae of about 50 nm. When (100) twins are present in high density, the electron diffraction patterns exhibit a strong streaking in the a^* directions of augite and pigeonite. The majority of twin lamellae are a few unit-cells thick, but some can be much thicker, up to 30 nm. Most of them are continuous across augite/pigeonite interfaces, but it can be seen that some of them terminate near the contact of a pigeonite/augite interface. Similar to the behavior of dislocations, twins can interact strongly with the strain field that accommodates the pigeonite and augite structures. Shearing displacement, clearly observed when twins cross augite/pigeonite lamellae (Fig. 7c), is closely proportional to the twin thickness. In areas of high twin density, the associated plastic deformation can reach up to 10%.

Twinning was also detected oriented parallel to (001) (Fig. 8a). On electron diffraction patterns, reflections according to the mirror twin law (001) are present. These (001) twins are much thicker than the (100) twins (typically 0.3–0.5 μm). We found only a few of them in the pyroxene grains we studied. As previously reported by Müller (1993) in the Shergotty meteorite, (001) twins concern only augite and affect the whole lamellae, i.e., the boundaries of the twins are also the plane augite/pigeonite interfaces. These twins all contain a high density of (100) stacking faults, with an average spacing of 20 nm. It is interesting to note that (001) twins are not sheared by the (100) twins. In addition, (100) twins are found to terminate on the (001) twins (Fig. 8a).

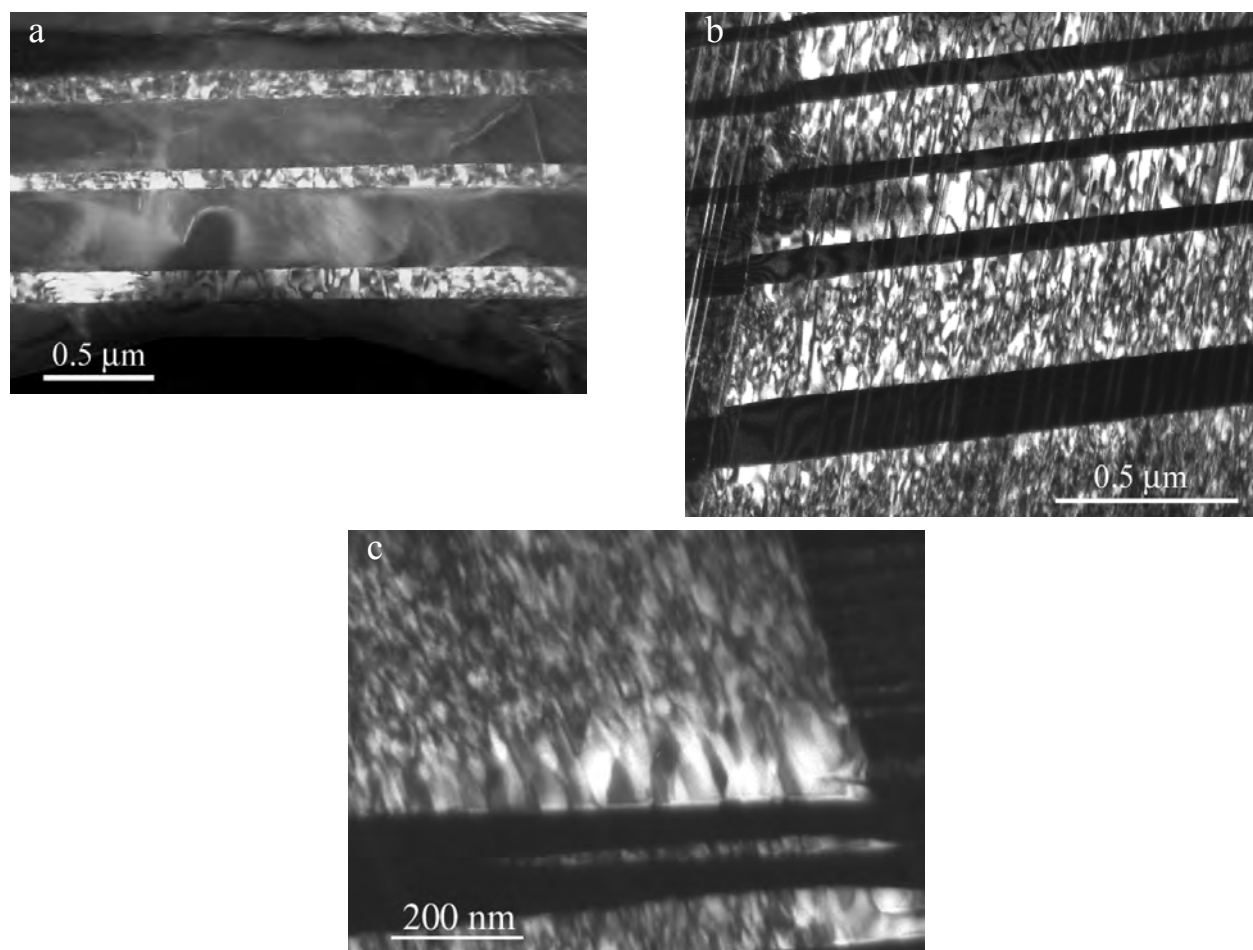


Fig. 5. TEM dark field images showing antiphase boundaries in pigeonite: a) pigeonite lamellae in an augite-rich grain. Image recorded using the 002 diffraction spot. The APBs appear as ribbons with more or less contrast depending on their boundary orientation; b) APD in a pigeonite-rich grain containing augite lamellae. Image recorded using the 302 reflection. Pigeonite is bright and augite lamellae are black since the 302 reflection ($h + k = \text{odd}$) only arises from pigeonite. This area also contains a high density of (100) twins; c) antiphase domains are often more coarse near the augite/pigeonite interfaces. Imaged with the reflection 302.

These observations clearly demonstrate that (001) twins are formed before (100) twinning.

DISCUSSION

Thermal History

The complex subsolidus microstructure of pyroxene minerals is useful to decipher the thermal evolution of their parent rock. In particular, the microstructure development strongly depends on the cooling rate. Below, we describe the thermal evolution of the NWA 856 pyroxenes that we studied by analytical TEM.

During crystallization of the parent magma, augite and pigeonite co-precipitated. Since liquidus temperatures are higher for Mg-rich pyroxenes, crystallization began with Mg-rich pyroxenes (typically $\text{En}_{45}\text{Wo}_{33}\text{Fs}_{22}$ for augite and $\text{En}_{58}\text{Wo}_{13}\text{Fs}_{29}$ for pigeonite; Jambon et al. 2002) and evolved toward Fe-rich compositions (typically $\text{En}_{30}\text{Wo}_{30}\text{Fs}_{40}$ for

augite and $\text{En}_{35}\text{Wo}_{15}\text{Fs}_{40}$ for pigeonite; Jambon et al. 2002), resulting in zoned pyroxenes with Mg-rich cores surrounded by Fe-rich rims. According to the pyroxene phase diagram (Lindsley 1983; Sack and Ghiorso 1994), crystallization started by Mg-rich pyroxene at temperatures between 1200 and 1100 °C. Crystallization was completed about 50 °C lower by the Fe-rich rims, i.e., at about 1100 °C. The fact that the Fe-Mg zoning is not obliterated indicates a relatively fast cooling of the parent magma.

At the time of their formation, high temperature augite and pigeonite both crystallized in the C2/c space group. Cooling led to the development of augite/pigeonite exsolutions on (001) in both augite and pigeonite primary grains. Exsolutions are formed when augite (or pigeonite) enters the two phase field augite + pigeonite, after crystallization. This is the reason that lamellae are usually found to be more coarse in the cores and finer in the rims of the grains (e.g., Brearley [1991] for the Zagami shergottite). Indeed, pyroxene cores are formed at higher temperature than

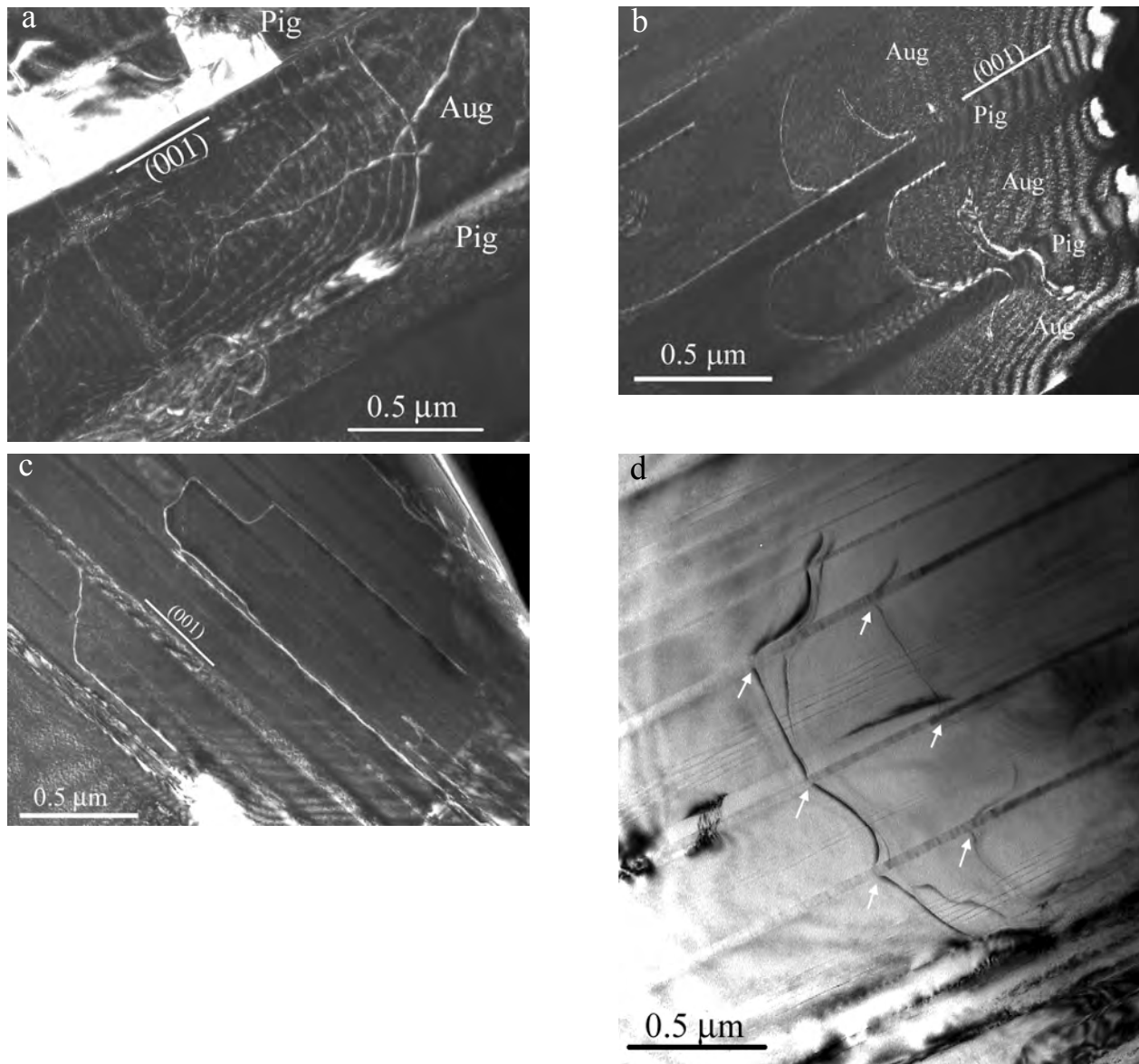


Fig. 6. Dislocation microstructure. All images are in the zone axis near $[100]$: a) dark field image with $g = 002$ of a dislocation source; b and c) dark field images taken with the 002 reflection showing typical dislocation configuration and augite/pigeonite intergrowths in (001). Note that the dislocations are frequently found straight in the augite/pigeonite interfaces; d) dislocation interaction with pigeonite lamellae (arrowed). Bright field image, reflection 002.

pyroxene in the rims. Exsolution mechanisms in pyroxenes have been intensively studied, and many descriptions can be found in the literature (e.g.; Buseck et al. 1980; Skrotzki et al. 1991; Putnis 1992). Here, we summarize only the main characteristics relevant for the NWA 856 pyroxene microstructure. The evolution of augite and pigeonite compositions along the solvus curve can be seen on Fig. 2. The primary exsolution lamellae were formed by nucleation and growth. They are coherent with their host phase (remember that, at high temperature, both belong to the $C2/c$ space group and have close lattice parameters). While temperature decreases, the augite and pigeonite unit cell parameters and their monoclinic β angles change at different

rates, causing increased strain at augite/pigeonite interfaces. It must be mentioned that coarsening was not associated with loss of coherence. Strain relaxation did not occur during cooling, contrary to the number of terrestrial augite-pigeonite associations in which crystal defects, such as misfit dislocations at augite/pigeonite interfaces or stacking faults on (100) planes in augite lamellae, are formed to relieve the coherency strain stored at the interfaces (e.g., Skrotzki et al. 1991; Putnis 1992).

Exsolution phenomena are controlled by temperature and time, thus providing information for the cooling history of the rock in the considered temperature interval. In particular, thickness and spacing of exsolution lamellae can be used for

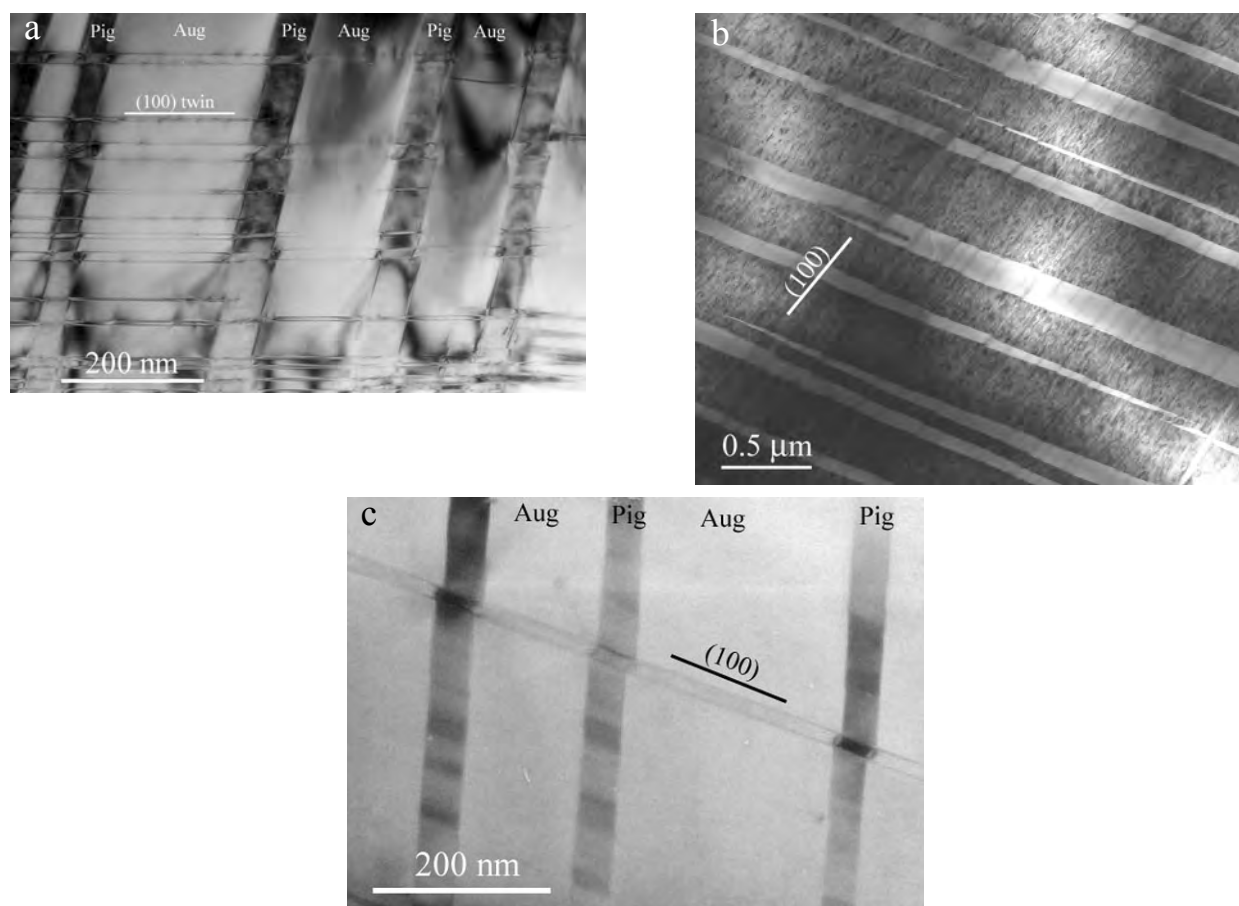


Fig. 7. Twin microstructure on (100). These bright field images were all taken with the plane orientation of the sample nearly perpendicular to [010]: a) twins on (100) crossing pigeonite lamellae; b) high density of (100) twin crossing through the (001) augite lamellae (in bright) in pigeonite (in dark). Note that the intersections of the twins with augite/pigeonite interfaces result in offsets of the lamellae, which give them a staggered appearance. This shear of the lamellae is found to be larger when the (100) twin bands are thicker. Twinning induced large plastic deformation; c) magnification of a (100) twin interacting with a pigeonite lamellae. Note that the lamellae are sheared. Note also the dark and bright contrast in the pigeonite lamellae, which is due to antiphase domains, here preferentially oriented parallel to (100).

cooling rate determination (e.g.; McCallister 1978; Grove 1982; Fukada et al. 1987; McCallum and O'Brien 1996; Weinbruch et al. 2001). According to Grove (1982), lamellae coarsening occurred within the first 200 °C of the continuous cooling process. That means that coarsening is almost completed at temperatures of about 900–1000 °C. Using the experimental data (exsolution wavelength vs cooling rate) for Fe-bearing clinopyroxenes determined by Grove (1982), Fukada et al. (1987), and Weinbruch et al. (2001), we infer cooling rates well below 0.1 °C/hr within the temperature interval 1150–950 °C. By comparison with experimental thermal annealing at constant temperature for comparable starting pyroxene composition (Nord and McCallister 1979), for which the spacing of the lamellae is proportional to (annealing time)^{1/3}, the width and wavelength of augite/pigeonite lamellae would indicate a residence time of 30 yr at 1000 °C. However, these values are only indicative, since other temperature-time values could yield similar microstructures, and experimental values are difficult to extrapolate to

geological durations anyway. Pyroxene exsolution features (and, hence, cooling rate) in NWA 856 are comparable with those of other martian meteorites such as Zagami (Brearley 1991; Langenhorst and Poirier 2000) or Shergotty (Müller 1993). For augite, the solvus line significantly varies in the pyroxene quadrilateral, with a strong decrease of the Fe + Mg solubility with temperature (see Figs. 2a and 2b). The compositions of augite lamellae (typically En₃₀Wo₄₄Fs₂₆) indicate an equilibration temperature of about 700 °C, according to subsolidus phase relationships of augite and pigeonite (Lindsley 1983; Fig. 2). This equilibration temperature is well below the final temperature expected for significant coarsening (900 °C), showing that sub-μm-scale Ca-Fe, Mg diffusion was efficient for phase equilibration within the temperature range 900–700 °C.

Microstructure development also occurred within lamellae within the temperature range 900–700 °C, in particular, in augite. At these moderate temperatures, the distance of diffusion rapidly became less than the spacing

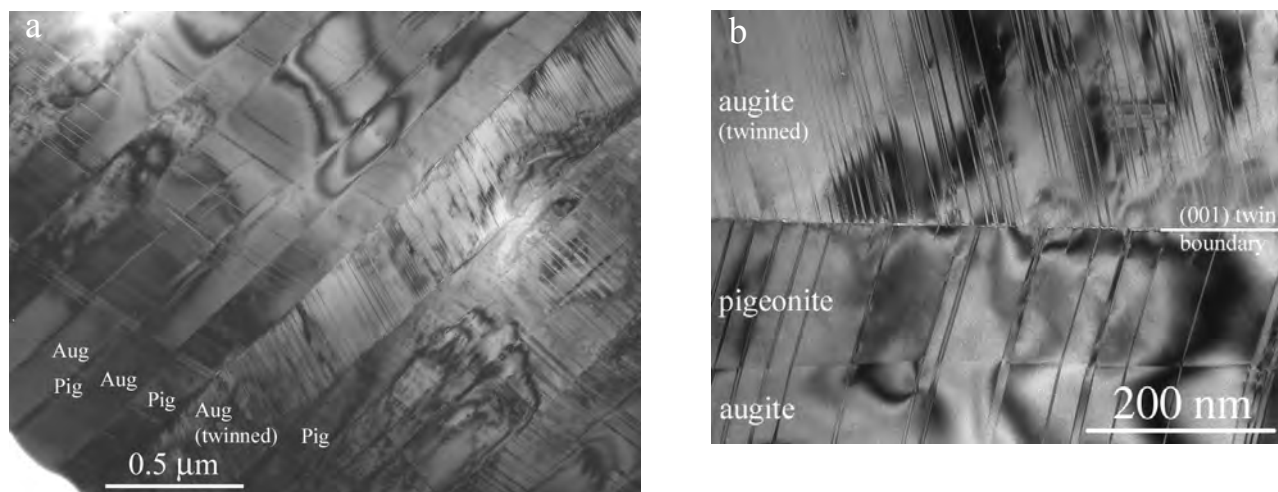


Fig. 8. Twin microstructure on (001). Bright fields images with grains oriented along a [010] zone axis: a) twinning on (001) in augite. Note the numerous stacking faults parallel to (100) in the twin lamellae; b) magnification of a (001) twin. (100) twins (upper part of the picture) are found to terminate on the (001) twin interface.

between lamellae. The sub- μm -scale Ca-Fe, Mg interdiffusion, thus, was not fast enough to maintain a full chemical equilibration between the two-phase assemblage, and the primary augite areas rapidly became metastable. Equilibrium was maintained only near the augite/pigeonite interfaces (where the diffusion distance was small). This deviation from equilibrium led to the development of a concentration profile in augite, with an augite/pigeonite interface composition close to the equilibrium composition and a supersaturation in Fe and Mg far from the interfaces (Fig. 4b). Similar “M-shaped” profiles are observed in a number of disequilibrium mineral associations, for instance, in taenite in iron meteorites (Goldstein and Ogilvie 1965). The supersaturated areas underwent spinodal decomposition when a critical supersaturation value was reached. Spinodal decomposition is a continuous mechanism that does not require a nucleation stage and proceeds from fluctuations of composition. Since lattice parameters and the monoclinic β angle are functions of composition (e.g., Cameron and Papike 1980), these fluctuations of composition induce elastic strain, which is revealed in TEM as a tweed texture, owing to fluctuating Bragg contrasts. When the compositional fluctuations were becoming large enough, formation of secondary pigeonite exsolution was possible on (001). It should be noted that, if (001) tweed succeeded in forming secondary exsolution, the (100) tweed failed to develop (100) lamellae. Such a behavior is frequently observed and is explained by the difference of elastic energies stored by the considered planes (Buseck et al. 1980). Numerous observations of such two-stage exsolution in Ca-rich clinopyroxene have been reported already (e.g., Buseck et al. 1980; Putnis 1992, and references therein for both). Finally, it is observed that areas near pigeonite interfaces do not display tweed structures nor contain secondary exsolution. In these areas, the critical concentration required to form secondary

exsolution was never reached. For similar reasons, a gradient in the width of pigeonite secondary exsolution is visible, with the coarser lamellae at the middle of augite bands where supersaturation was the highest (see Figs. 4a and 4b)

Pigeonite does not display secondary exsolution microstructure, which indicates that the phase transition from low-Ca clinopyroxene to orthopyroxene did not take place, suggesting a relatively rapid cooling rate below 950–1000 °C. This rapid cooling is also confirmed by the absence of (100) exsolution lamellae (in both augite and pigeonite). Owing to the displacive $C2/c$ to $P2_1/c$ phase transition, antiphase domains in pigeonite developed due to the loss of translational symmetry (see, for instance, Tribaudino [2000] for a detailed description of the $C2/c$ – $P2_1/c$ phase transition). Prewitt et al. (1971) studied the variation of the $C2/c$ – $P2_1/c$ transition temperature with comparable composition in lunar pigeonites. From their data, the transition temperature can be estimated to be in the range of 850–950 °C for pyroxenes in NWA 856 (Fig. 2b).

Shock History

At the TEM scale, the shock history of the meteorite is recorded in pyroxenes mainly by dislocations and twins.

For dislocations, the glide system $[001](100)$ was preferentially activated. This glide system is known to be the easiest one in clinopyroxene (e.g., Kirby and Christie 1977). It is typical of static deformation at moderate temperature and is also found to be predominant in shocked diopside in meteorites (Ashworth 1980; Langenhorst et al. 1995; Leroux 2001). Dislocations originated from areas of stress concentration, such as crack tips. Such formation mechanisms are frequent in silicates during shock deformation (Leroux et al. 1994, 1999; Langenhorst et al. 1999). It is to be noted that the dislocation density is not very

high, at least lower than in experimentally shocked diopside at 45 GPa (Leroux et al. 1994) or in diopside from the strongly shocked L6 Tenham chondrite (Langenhorst et al. 1995). We observed that the strained interfaces acted as obstacles to the propagation of the dislocations. Thus, plastic deformation due to dislocations is probably very low, since dislocations could not propagate over large distances.

The deformation of pyroxenes in NWA 856 is mainly due to (100) twinning. In some areas, the amount of plastic deformation due to these twins reaches values around 10%. This twinning is produced by the formation and glide of $1/2[001]$ partial dislocations on (100) planes (Kirby and Christie 1977). This mechanical twinning is well-known to induce deformation in clinopyroxenes at high strain rates and moderate temperatures (conditions including shock deformation). Previously, they have been characterized in diopside from mildly shocked meteorites (Ashworth 1980, 1985), in experimentally shocked diopside (Hornemann and Müller 1971; Leroux et al. 1994), in lunar pyroxene samples (e.g., Nord and McGee 1979), in martian meteorites (Müller 1993; Langenhorst and Poirier 2000), and also in static laboratory deformation experiments (Kirby and Christie 1977) or in tectonically deformed clinopyroxenes (Skrotzki 1995). The partial dislocations $1/2[001]$, similar to the perfect [001] dislocations, were observed to interact with the strain field that accommodates pigeonite and augite intergrowths. However, a number of [001] partial dislocations succeeded in passing the obstacles that are the augite/pigeonite strained interfaces.

The (001) twinning orientation is frequent in shocked clinopyroxene from meteorites (Ashworth 1985; Müller 1993; Langenhorst et al. 1995; Leroux 2001), as well as in experimentally shocked diopside (Hornemann and Müller 1971; Leroux et al. 1994). Twins on (001) also occur in static deformation at high strain rate and high deviatoric stress (Kirby and Christie 1977). They are formed by a massive cooperative movement of atoms (Kirby and Christie 1977). In general, they are believed (e.g., Leroux 2001) to be the signature of a strong shock event. Only few (001) twins were present in the studied pyroxene grains. We believe they are growth twins. They can result either from twinning in primary augite in which pigeonite exsolution precipitated or from twinning during the exsolution of augite lamellae in pigeonite. Thus, (001) twins would not be related to shock deformation. As already discussed, augite/pigeonite interfaces are coherently strained. If a twin lamella is present, the coherency is lost at twin boundaries. During cooling, augite and pigeonite cell parameters and β angles continuously deviate. At twin boundaries, the deviation can not be accommodated by elastic strain close to the interfaces. Change of orientation and strain relief are permitted by the generation of stacking faults on (100) planes in the twinned augite, with, presumably, $1/2[001]$ as the displacement vector. Twin lamellae are thus sheared into small segments delimited

by stacking faults. Such a relaxation process has been described in a number of exsolved clinopyroxenes (e.g., Robinson et al. 1977; Mori and Takeda 1988; Skrotzki et al. 1991; Putnis 1992).

Since all martian meteorites are found to be strongly shocked (Stöffler 2000), the NWA 856 meteorite was expected to defer to the same rule. This is confirmed by the presence of maskelynite, melt pockets, and stishovite (Jambon et al. 2002). However, at the TEM scale pyroxenes do not show evidence of really strong shock metamorphism. Indeed, mosaicism, amorphous shock lamellae, and mechanical (001) twinning are absent and microfracturing is rare, while such defects are found to occur in a number of strongly shocked clinopyroxenes (Ashworth 1985; Leroux et al. 1994; Langenhorst et al. 1995; Leroux 2001). Although several pyroxene grains in several TEM samples have been investigated, it is possible that the small piece of meteorite we have studied was less shocked than the rest of the meteorite. It is also possible that the composite microstructure of martian pyroxenes (fine-scaled pigeonite/augite alternation) make these minerals much more resistant to shock deformation compared to unexsolved clinopyroxenes. Unfortunately, to our knowledge, no experimental data is available from exsolved pyroxene behavior under shock.

Acknowledgments—The authors thank J. A. Barrat for supplying the meteorite sample. The authors thank Jean-François Dhénin for his assistance with TEM. This work was supported by the Institut National des Sciences de l'Univers (INSU) of the CNRS through the "Programme National de Planétologie" (PNP) and by the Centre National d'étude Spatiale (CNES). We thank D. J. Barber for a constructive review and A. H. Treiman for the editorial handling. TEM work was performed at the French INSU National Facilities for electron microscopy at LSPES, Lille, and CRMC2, Marseille.

Editorial Handling—Dr. Allan Treiman

REFERENCES

- Ashworth J. R. 1980. Deformation mechanisms in mildly shocked chondritic diopside. *Meteoritics* 15:105–115
- Ashworth J. R. 1985. Transmission electron microscopy of L-group chondrites, I: Natural shock effects. *Earth and Planetary Science Letters* 73:17–32.
- Brearley A. J. 1991. Subsolidus microstructures and cooling history of pyroxenes in the Zagami shergottite (abstract). Proceedings, 22th Lunar and Planetary Science Conference. pp. 135–136.
- Buseck P. R., Nord G. L., Jr., and Veblen D.V. 1980. Subsolidus phenomena in pyroxenes. In *Reviews in mineralogy, volume 7: Pyroxenes*, edited by Prewitt C. T. Washington D.C.: Mineralogical Society of America. pp. 117–211.
- Carpenter M. A. 1979. Contrasting properties and behavior of antiphase domains in pyroxenes. *Physics and Chemistry of Minerals* 5:119–131.
- Cameron M. and Papike J. J. 1980. Crystal chemistry of silicate

- pyroxenes. In *Reviews in mineralogy, volume 7: Pyroxenes*, edited by Prewitt C. T. Washington D.C.: Mineralogical Society of America. pp. 5–87.
- Fukada K, Yamanaka T., and Takonami N. 1987. Dependence of exsolution textures in synthetic augite on its composition and cooling rate. *Mineralogical Journal* 13:376–389.
- Goldstein J. I. and Ogilvie R. E. 1965. The growth of Widmanstätten pattern in metallic meteorites. *Geochimica Cosmochimica Acta* 29:893–920
- Grove T. L. 1982. Use of exsolution lamellae in lunar clinopyroxenes as cooling rate speedometers: An experimental calibration. *American Mineralogist* 67:251–268.
- Hornemann U. and Müller W. F. 1971. Shock-induced deformation twins in clinopyroxene. *Neues Jahrbuch fuer Mineralogie—Monatshefte* 6:247–255.
- Jambon A, Barrat J. A., Sautter V., Gillet P., Göpel C., Javoy M., Joron J. L., and Lesourd M. 2002. The basaltic shergottite Northwest Africa 856: Petrology and chemistry. *Meteoritics & Planetary Science* 37:1147–1164.
- Kirby S. H. and Christie J. M. 1977. Mechanical twinning in diopside, (Ca, Mg)₂Si₂O₆: Structural mechanism and associated crystal defects. *Physics and Chemistry of Minerals* 1:137–163.
- Langenhorst F., Joreau P., and Doukhan J. C. 1995. Thermal and shock metamorphism of the Tenham chondrite: A TEM examination. *Geochimica et Cosmochimica Acta* 59:1835–1845.
- Langenhorst F., M. Boustie M., Migault A., and Romain J. P. 1999. Laser shock experiments with nanoseconds pulses: A new tool for the reproduction of shock defects in olivine. *Earth and Planetary Science Letters* 173:333–342.
- Langenhorst F. and Poirier J. P. 2000. Anatomy of black veins in Zagami: Clues to the formation of high-pressure phases. *Earth and Planetary Science Letters* 184:37–55.
- Leroux H., Doukhan J. C., and Langenhorst F. 1994. Microstructural defects in experimentally shocked diopside: A TEM characterization. *Physics and Chemistry of Minerals* 20:521–530.
- Leroux H., Reimold W. U., Koeberl C., Hornemann U., and Doukhan J. C. 1999. Experimental shock deformation in zircon: A transmission electron microscope study. *Earth and Planetary Science Letters* 169:291–301.
- Leroux H. 2001. Microstructural shock signatures of major minerals in meteorites. *European Journal of Mineralogy* 13:253–272.
- Lindsley D. H. 1983. Pyroxene thermometry. *American Mineralogist* 68:477–493.
- McCallister R. H. 1978. The coarsening kinetics associated with exsolution in a iron-free clinopyroxene. *Contributions to Mineralogy and Petrology* 65:327–331
- McCallum I. S. and O'Brien H. E. 1996. Stratigraphy of the lunar highland crust: Depths of burial of lunar samples from cooling-rate studies. *American Mineralogist* 81:1166–1175.
- Miyamoto M., Mikouchi T., and K. Kaneda K. 2001. Thermal history of the Ibitira noncumulate eucrite as inferred from pyroxene exsolution lamella: Evidence for reheating and rapid cooling. *Meteoritics & Planetary Science* 36:231–237
- Mori H. and Takeda H. 1988. Stress induced transformation of pigeonite from achondrite meteorites. *Physics and Chemistry of Minerals* 15:252–259.
- Morimoto N. and Tokonami M. 1969. Domain structure of pigeonite and clinoenstatite. *American Mineralogist* 54:725–740.
- Muir I. D. 1954. Crystallization of pyroxenes in an iron-rich diabase from Minnesota. *Mineralogical Magazine* 30:376–388.
- Müller W. F. 1991. Microstructure of minerals in a chondrule from the Allende meteorite II. Thermal history deduced from clinopyroxene and other minerals. *Neues Jahrbuch für Mineralogie—Abhandlungen* 163:145–158.
- Müller W. F. 1993. Thermal and deformation history of the Shergotty meteorite deduced from clinopyroxene microstructure. *Geochimica et Cosmochimica Acta* 57:4311–4322.
- Nord G. L., Jr. and McCallister R. H. 1979. Kinetics and mechanism of decomposition in Wo₂₅En₃₁Fs₄₄ clinopyroxene (abstract). *Geological Society of America Abstracts with Program* 11:488.
- Nord G. L., Jr. and McGee J. J. 1979. Thermal and mechanical history of granulite norite and pyroxene anorthosite clasts in breccia 73255. Proceedings, 10th Lunar and Planetary Science Conference. pp. 817–832.
- Prewitt C. T., Brown G. E., and Papike J. J. 1971. Apollo 12 clinopyroxenes: High temperature X-ray diffraction studies. Proceedings, 2nd Lunar and Planetary Science Conference. pp. 59–68.
- Putnis A. 1992. *Introduction to mineral sciences*. Cambridge: Cambridge University Press. 457 p.
- Robinson P., Ross M., Nord G. L., Jr., Smyth J. R., and Jaffe H. W. 1977. Exsolution lamellae in augite and pigeonite: Fossil indicators of lattice parameters at high temperature and pressure. *American Mineralogist* 62:857–873.
- Sack R. O. and Ghiorso M. S. 1994. Thermodynamics of multicomponent pyroxene: II. Phase relation in the quadrilateral. *Contributions to Mineralogy and Petrology* 116:287–300.
- Skrotzki W., Müller W. F., and Weber K. 1991. Exsolution phenomena in pyroxenes from the Balmuccia massif, NW-Italy. *European Journal of Mineralogy* 3:39–61.
- Skrotzki W. 1995. Defect structure and deformation mechanisms in naturally deformed augite and enstatite. *Tectonophysics* 229:43–68.
- Stöffler D. 2000. Maskelynite confirmed as diaplectic glass: Indication for peak shock pressures below 45 GPa in all martian meteorites (abstract #1170). 31st Lunar and Planetary Science conference. CD-ROM.
- Tribaudino M. 2000. A transmission electron microscope investigation of the C2/c → P2₁/c phase transition in clinopyroxene along the diopside-enstatite (CaMgSi₂O₆-Mg₂Si₂O₆) join. *American Mineralogist* 85:707–715.
- Van Cappellen E. 1990. The parameterless correction method in X-ray microanalysis. *Microscopy Microanalysis Microstructure* 1: 1–22.
- Van Cappellen E. and Doukhan J. C. 1994. Quantitative transmission X-ray microanalysis of ionic compounds. *Ultramicroscopy* 53: 343–349.
- Weinbruch S., Müller W. F., and Hewins R. H. 2001. A transmission electron microscope study of exsolution and coarsening in iron-bearing clinopyroxene from synthetic analogues of chondrules. *Meteoritics & Planetary Science* 36:1237–1428.
- Yamakawa M. 1971. Two different crystallization trends of pyroxene in a tholeiitic dolerite, Semi, northern Japan. *Contributions to Mineralogy and Petrology* 33:232–238.
- Zema M., Domeneghetti C. M., Molin, G. M., and Tazzoli V. 1997. Cooling rates of diogenites: A study of Fe²⁺-Mg ordering in orthopyroxene by X-ray single-crystal diffraction. *Meteoritics & Planetary Science* 32:855–862.